FINAL REPORT: GRANT DOE DE-FG02-04ER54768

(Dated: January 11, 2016)

Abstract

The magnetized spherical implosion campaign funded by this grant is summarized in this progress report. The main goal of this grant was to improve the seed field generator MIFEDS (Magneto-Inertial Fusion Energy Delivery System) on the OMEGA laser to enable experiments at high fields (> 8 T) and to carry out magnetized spherical implosion experiments to study the effect of magnetic fields on the fusion yield. New experiments were carried out in the last budget period to study the effect of higher fields and shaped laser pulses. These new experiments improved the magnetized implosion database and allowed us to improve the confidence of our conclusions with respect to the effect of magnetic fields on implosion performance. The main conclusion is that adding magnetic field leads to a 30% higher neutron yield, but using seed magnetic field higher than 8 T does not further increase the neutron yield. A further conclusion is that the yield enhancement due to the magnetic field is approximately independent of the laser pulse shape.

I. INTRODUCTION

In inertial confinement fusion (ICF), a shell of cryogenic deuterium (D) and tritium (T) ice is imploded by irradiating the target either directly with lasers (direct-drive) or with x-rays generated by lasers (indirect-drive). The outer layer absorbs the radiation and ablates, generating a pressure of the order of tens of Mega-bar that implodes the shell at high velocities ($V_{\rm i} \sim 3 - 4 \times 10^7$ cm/s). As the shell implodes, the gas is compressed and its pressure increases, finally causing the imploding shell to stagnate. At stagnation, the gas at the center forms a hot spot with a temperature ($T_{\rm hs}$) of the order of several keV, high enough that deuterium and tritium fuse, creating alpha particles and neutrons. If the hot spot areal density is high enough, alpha particles are stopped in the hot spot, depositing their energy and heating it. If the deposited energy exceeds the energy lost due to thermal conduction and radiation, the target ignites; a burn wave propagates outward, heating the dense shell leading to more nuclear fusion reactions. Finally, the target explodes, cools down and the whole process ends.

To achieve ignition, a high hot spot temperature is required, which requires a fast implosion to compensate the thermal losses. The scaling law from Ref. [1] shows that $T_{\rm hs} \sim V_{\rm i}^{1.4}$. On the other hand, the energy gain in direct-drive ICF $G = E_{\rm TN}/E_{\rm L}$ is less with higher implosion velocity, where $E_{\rm TN}$ and $E_{\rm L}$ are the thermonuclear burn energy and deposited laser energy, respectively. It is shown in Ref. [1] that $G \sim \eta_{\rm h} V_{\rm i}^{-2}$ where $\eta_{\rm h}$ is the hydrodynamic efficiency given by $\sim V_{\rm i}^{0.75} I_{\rm L}^{-0.25}$, where $I_{\rm L}$ is the laser intensity. To achieve a high hot spot temperature but remain at high gain, a slow implosion with low heat conduction is required. One alternative approach to ICF is to reduce the thermal losses by magnetizing the plasma. The technique of adding magnetic fields to ICF implosions is called magneto-inertial confinement fusion (MIF).

When the plasma is magnetized, the electron-cyclotron frequency $\omega_{\rm ce}$ exceeds the collision frequency $\nu_{\rm e}$, i.e., $\omega_{\rm ce}\tau_e >> 1$ where $\tau_{\rm e} = \nu_{\rm e}^{-1}$ is the collision time. In other words, the electron Larmor radius $R_{\rm L}$ is shorter than the electron mean free path $l_{\rm mfp}$. For a typical hot spot density of ~ 10 g/cc and temperature of ~ 5 keV, a magnetic field $B > 10$ MG is required. If one would like to confine the 3.5 MeV alpha particles produced in the D + T fusion reactions, the Larmor radius of the alpha-particles must be smaller than the hot spot radius, $R_{\rm h}$, which is typically ~ 40 μm, a magnetic field exceeding ~ 90 MG is then needed.

Such a high field can not be externally applied. Fortunately, since the gas fill of an ICF target is quickly ionized by the shocks propagating through the targets, the ionized gas becomes a good conductor and traps magnetic flux. As the shell implodes, the density as well as the field are compressed to keep the flux approximately constant, i.e., the magnetic field increases as the radius decreases. In the ideal case where the flux is conserved, the magnetic field at stagnation is $B_{\rm max} \sim C^2$, where $C \equiv R_{\rm I}/R_{\rm stag}$ is the convergence ratio, $R_{\rm I}$ and $R_{\rm stag}$ are the initial shell radius and radius at stagnation, respectively. In reality, some of the flux is lost due to diffusion. In this case, the magnetic field at stagnation is $B_{\rm max} \sim C^{2(1-1/R_{\rm m})}$ where $R_{\rm m} \sim 50$ is the time-averaged magnetic Reynolds number [2]. Previous experiments funded by this grant have shown that a field more than tens of MG can be achieved [3], which is high enough to magnetize the hot spot. Nevertheless, the magnetic pressure is only ~ 4 GBar, which is much smaller than the thermal pressure in a regular ICF target (tens of GBar on OMEGA experiments and hundreds of GBar on NIF experiments), i.e., the ratio of thermal pressure to the magnetic pressure $\beta >> 1$. In addition, previous experiments supported by this grant have shown that the neutron yield and the ion temperature increase by 30 % and 15 %, respectively, in a magnetized, spherical target [4].

In this report, suppression of electron thermal conductivity due to magnetization is discussed in section II, using Braginskii's formalism [5]. In section III, numerical simulations for OMEGA experiments are provided, using a 1.5-dimensional, resistive-magnetohydrodyanmic code, LILAC-MHD [6], where the hydrodynamics is one dimensional (1D) while the magnetic field is two dimensional (2D). Section IV describes the configuration of the experiments on the Omega Laser facility [7] at the Laboratory for Laser Energetics, University of Rochester, Rochester, NY. The results of all experiments, including the most recent experiments, are summarized in section V and the conclusions in given in section VI.

The most recent publication of results from this grant appeared in 2015 in Physics of Plasmas: J. R. Davies *et al*, *The importance of electrothermal terms in Ohm's law for magnetized spherical implosions*, Physics of Plasmas 22, 112703. Another paper by P.-Y. Chang *et al, Parameter scan for magnetized inertial confinement fusion (MagICF)* is currently under internal review and will be submitted to Physics of Plasmas within the next few weeks.

II. THERMAL CONDUCTIVITY REDUCTION

When plasma is magnetized, thermal conductivity perpendicular to the magnetic field lines is suppressed. The suppression can be quantified using the Hall parameter χ, defined as $\omega_{\rm ce}\tau_{\rm e}$. Using Braginskii's formalism [5], the heat flux in the electron energy equation

$$\frac{3}{2}n_{\rm e}\left(\frac{\partial}{\partial t}+\overrightarrow{v_{\rm e}}\cdot\nabla\right)T_{\rm e}+p_{\rm e}\nabla\cdot\overrightarrow{v_{\rm e}}=-\nabla\cdot\overrightarrow{q_{\rm T}^{e}}+Q_{\rm e} \tag{1}$$

can be written as

$$\overrightarrow{q_{\rm T}^{e}}=-\kappa_{||}^{e}\nabla_{||}T_{\rm e}-\kappa_{\perp}^{e}\nabla_{\perp}T_{\rm e}-\kappa_{\wedge}^{e}\hat{B}\times\nabla T_{\rm e} \tag{2}$$

where

$$\kappa_{||}^{e}=\frac{n_{\rm e}T_{\rm e}\tau_{\rm e}}{m_{\rm e}}\gamma_0\ ,\ \kappa_{\perp}^{e}=\kappa_{||}^{e}\left(\frac{1}{\gamma_0}\frac{\gamma_1'\chi^2+\gamma_0'}{\chi^4+\delta_1\chi^2+\delta_0}\right)\equiv\kappa_{||}^{e}\ \kappa_B\ ,\ \kappa_{\wedge}^{e}=\kappa_{||}^{e}\frac{1}{\gamma_0}\frac{\chi\left(\gamma_1''\chi^2+\gamma_0''\right)}{\chi^4+\delta_1\chi^2+\delta_0}\ . \tag{3}$$

Constants γ_0 , γ_0', γ_1', γ_0'', γ_1'', δ_0, δ_1 are defined in Ref. [5] and $Q_{\rm e}$ is the heat exchange between electrons and ions. In Eq. 1, $n_{\rm e}$, $T_{\rm e}$, $\overrightarrow{v_{\rm e}}$ and $m_{\rm e}$ are the number density, temperature, velocity and mass of electrons, respectively. Note that the third term in Eq. 2 does not change the temperature profile in a perfect spherical implosion with an embedded seed magnetic field in the z-direction due to the azimuthal symmetry. For DT gas, $\kappa_{\perp}^{e}$ is reduced by 73 % when $\chi = 1$ and by 96 % when $\chi = 5$. However, heat can flow along field lines, .i.e., $\kappa_{||}^{e}$ is unaffected by magnetic field. Using a geometric factor $\zeta \equiv A_{\perp}/A_{||}$, where $A_{\perp}$ and $A_{||}$ are the projected areas of the hot-spot in the directions perpendicular and parallel to the field lines, respectively, the total thermal conductivity can be written $\kappa_{\rm tot} = \kappa_{||}^{e}\left(1+\zeta\kappa_B\right)/\left(1+\zeta\right)$. In a perfectly spherical target with straight magnetic field lines $A_{\perp} = A_{||}$ leading to $\zeta = 1$. With a strong magnetic field such that $\kappa_{\rm B} = 0$, $\kappa_{\rm tot}$ can at most be halved. Since temperature scales as $\kappa_{\rm tot}^{-2/7}$ [8], the expected increase in $T_{\rm e}$ is a factor of $2^{2/7} = 1.22$. Neutron yield $Y_{\rm n} \propto n^2\left\langle\sigma v\right\rangle Vt \propto p^2T^2Vt$, since $\left\langle\sigma v\right\rangle \propto T^4$ in the temperature range of 2 – 5 keV, and hot spot pressure p, volume V and confinement time t are not expected to change significantly with magnetization, so a temperature increase by a factor of 1.22 should increase neutron yield by a factor of 1.49.

III. NUMERICAL SIMULATION

OMEGA experiments were simulated using a 1.5-dimensional, resistive-magnetohydrodyanmic (MHD) code, LILAC-MHD, funded by this grant under previous budget periods. The code is based on the 1D, Lagrangian radiation-hydrodynamic code LILAC [9] developed at the Laboratory for Laser Energetics (LLE). LILAC includes SESAME [10] equation of state tables, flux-limited Spitzer thermal conduction, multi-group radiation transport, multi-group alpha-particle transport, and 3D laser ray-tracing. A resistive-MHD package, including the Nernst term [11], was added to LILAC under the support of this grant. Note that the magnetic field is only compressed in the direction perpendicular to the field lines. In a perfect implosion without perturbation, the topology of the compressed field lines becomes two-dimensional while keeping azimuthal symmetry. In place of a full two-dimensional simulation, a one-and-a-half-dimensional simulation where the magnetic field is simulated in two dimensions while the hydrodynamics remains in one dimensional is used. This is a reasonable approximation provided that $\beta >> 1$, so magnetic pressure does not modify the hydrodynamics, and that loss of symmetry in the thermal conductivity does not significantly modify the hydrodynamics. X-ray back-lighted images taken a few 100 ps before peak compression have shown that embedding a magnetic field in a spherical target does not affect the uniformity of the shell [4].

In the simulations, the hydrodynamic quantities are one-dimensional (depending only on r) while the magnetic field depends on r and θ and is in the $\hat{r}$ and $\hat{\theta}$ directions. The azimuthal component B_ϕ remains 0 with the assumption of azimuthal symmetry. The induction equation is solved in vector potential form

$$\frac{\partial \vec{A}}{\partial t} = \vec{v} \times \left(\nabla \times \vec{A} \right) - \frac{\eta}{\mu_0} \nabla \times \left(\nabla \times \vec{A} \right) \tag{4}$$

where η is resistivity, $\vec{v}$ is fluid velocity, and only the azimuthal component A_ϕ is needed. Magnetic field convection due to the heat flow, the Nernst effect, is also included in the code. It is due to the friction force R_{u} given by Braginskii [11] as

$$\frac{\partial \vec{B}}{\partial t} = -\frac{c}{e}\nabla \times \left(\frac{\vec{R}_{\rm T}}{n_{\rm e}}\right) \tag{5}$$

$$\vec{R}_{\rm T} = -\beta_{||}\nabla_{||}T_{\rm e} - \beta_{\perp}\nabla_{\perp}T_{\rm e} - \beta_{\wedge}\hat{B}\times\nabla T_{\rm e} \tag{6}$$

$$\beta_{||} = \beta_0 n_{\rm e} \quad , \quad \beta_{\perp} = n_{\rm e}\frac{\beta_1'\chi^2+\beta_0'}{\Delta} \equiv n_{\rm e}\hat{\beta}_{\perp} \quad , \quad \beta_{\wedge} = n_{\rm e}\frac{\chi\left(\beta_1''\chi^2+\beta_0''\right)}{\Delta} \equiv n_{\rm e}\chi\hat{\beta}_{\wedge} \quad .$$

Similar to the induction equation, the additional convection can be written using the vector potential as follows in the case where the hydrodynamics is only in the $\hat{r}$ direction.

$$\frac{\partial A_\phi}{\partial t} = -V_{\rm T}\frac{1}{r}\frac{\partial}{\partial r}\left(rA_\phi\right) \tag{7}$$

$$V_{\rm T} = -\frac{\tau}{m}\left(\frac{\beta_1''\chi^2+\beta_0''}{\Delta}\right)\frac{\partial T}{\partial r} \tag{8}$$

where $V_{\rm T}$ is called the Nernst velocity. It has been demonstrated that the Nernst velocity significantly modifies magnetic field compression for our parameters [12].

Magnetic fields change the hydrodynamics through the $\vec{j}\times\vec{B}$ force, Ohmic heating and reduction of the heat flow. The $\vec{j}\times\vec{B}$ force is calculated directly using A_ϕ. Since the hydrodynamic part is only calculated in 1D, only the radial force is used and computed in the code. The current density $\vec{j}$ used in the Ohmic heating is calculated using Ampere's law. For the reduction of the heat flow, since the magnetic field is not necessary parallel or perpendicular to the heat flow which is only in the radial direction in the code, an effective heat conduction is calculated as follows:

$$\kappa^e_{\rm eff} = \kappa^e_{||}\left(\cos^2\theta + \sin^2\theta\ \kappa_{\rm B}\right) \quad , \tag{9}$$

where θ is the angle between the magnetic field line and the heat flow. For all variables related to magnetic field, averages in $\hat{\theta}$ need to be taken for the hydrodynamics calculation.

Another modification to the code is the flux limiter in the gas region. The flux limiter is required when the temperature gradient is so steep that the scale length for temperature variation is shorter than the electron mean free path, and the characteristic speed of the heat flow becomes larger than the electron thermal velocity. Although a steep ion temperature gradient forms across the shock front, the electron temperature should be smooth due to the longer mean free path. Therefore, the electron flux limiter in the gas region is set to unity. This approach is described in more detail in Ref. [12].

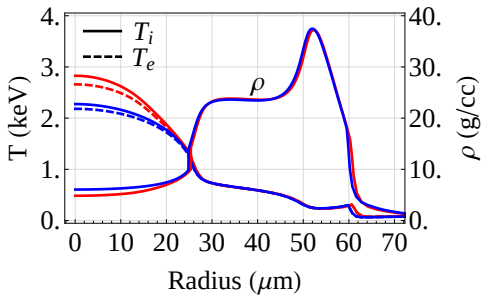

Figure 1. Comparison of the simulation results at stagnation ($\sim$ 2.2 ns) for $B_0 = 15, 0$ T. The solid lines and dashed lines represent the ion and electron temperature, respectively. The red and blue lines are for $B_0 = 15, 0$ T, respectively.

Shown in Fig. 1 are the simulation results of one of the experimental conditions where a spherical plastic (CH) target, 22 μm thick, 862.2 μm in outer diameter, and filled with 10.1 atm D_2 gas is imploded using a 1 ns square pulse delivering 16.7 kJ of laser energy on target. A 15 T seed magnetic field along the pole ($\hat{z}$ direction) is imposed before the implosion. Another simulation for the same conditions but without field is shown in the same figure for comparison. Both electron and ion temperature increase due to reduction of the thermal conductivity. The shell position, however, does not change, meaning the compression is not influenced directly by the magnetic field. The neutron-averaged ion temperature increases from 2.17 keV to 2.53 keV (+17 %) and the neutron yield increases from 9.21×10^{10} to 12.4×10^{10} (+35 %).

Shown in Fig. 2 are 2D spatial profiles close to the end of the laser pulse ($\sim$ 0.8 ns). The magnetic field can only be convected by the plasma in the direction perpendicular to the field lines, i.e., on the equatorial plane. The magnetic field in the gas region is compressed by the imploding shell while the field outside the shell is stretched by the ablated plasma, causing it to decrease. The thermal conductivity between the ablation surface (white circle) and the critical surface (purple circle) is practically unaffected by the magnetic field, so the magnetic field outside the ablation surface should not change the ablated pressure nor the implosion velocity.

Shown in Fig. 3 are the plots at stagnation at $\sim$ 2.2 ns. The peak magnetic field in the hot spot is compressed to over 5000 T. About 80 % of the initial flux in the gas region is conserved. The hot spot pressure is $\sim$ 12.8 GBar and the average magnetic field in the hot spot is $\sim$ 3100 T giving $\beta \sim 340$. This confirms the approximation $\beta >> 1$

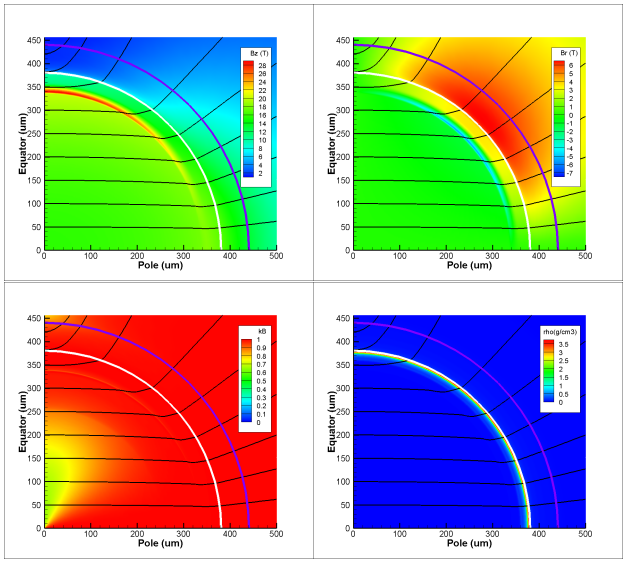

Figure 2. Spatial profile of (a) Bz (T), (b) Br(T), (c)$\kappa_{\rm B}$, and (d) $\rho\left({\rm g/cm^3}\right)$ at the end of the laser pulse at 1 ns. The white and the purple circle in the plots are the ablation and critical surface, respectively. The black lines are the field lines.

and the hydrodynamic compression is not influenced directly by the magnetic field. Since the magnetic field can only be convected in the direction perpendicular to the field lines, the field lines are squeezed on the equatorial plane leading to a dipole-like topology. The thermal conductivity in the hot spot is reduced, i.e., $\kappa_{\rm B} << 1$, only in the region close to the equatorial plane where the magnetic field is large and the field lines are perpendicular to the direction of the temperature gradient. The average of the effective thermal conductivity $\kappa^e_{\rm eff}$ given by Eq. 9 is ~ 0.36 at the center and increases to 1 at the hot spot boundary. This is slightly better than the estimate of the projected area perpendicular to the field lines being half of the total hot spot area assuming straight field lines.

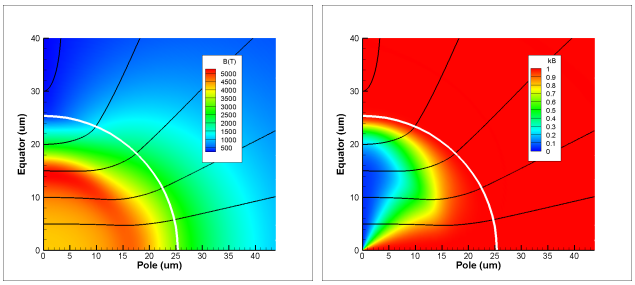

Figure 3. Spatial profile of (a) B (T) and (b) $\kappa_{\rm B}$ at stagnation at ~ 2.2 ns. The white circle in the plots are the hot spot radius. The black lines are the field lines.

IV. EXPERIMENTAL CONFIGURATION

Targets used in the experiments were spherical plastic (CH) shells with approximately 860 and 920 μm outer diameters and 21.5 to 24.5 μm thick. The implosions were driven by 40 OMEGA laser beams in polar drive (PD) configuration [13, 14] with smoothing by spectral dispersion (SSD) and distributed polarization rotators (DPRs). The laser spot sizes were 860 μm on target using SG4 phase plates. In the PD configuration, there are five beams in each rings 1 and 2 (top and bottom) and ten beams in rings 3 (top and bottom). Rings 1, 2, and 3 were offset from the target center by 90, 180, and 180 μm perpendicular to the beam axis, respectively [15]. The configuration gives adequate implosion symmetry despite the non-spherical irradiation pattern [4, 16]. To provide the seed magnetic fields, single coils, shown in Fig. 4, on the equatorial plane of the target were used. In the first experiments, copper foil was used to make the coils (Type I) [17]. In later experiments, kapton coated copper wire wound around a 3D printed plastic frame was used (Type II and III) [18].

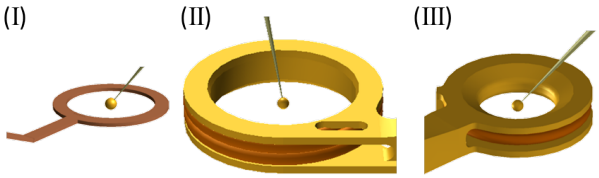

Figure 4. (I) single coil, Cu foil, B = 8 T; (II) single coil, 3D printed, square, B = 8, 9 T; (III) single coil, 3D printed, diamond, B = 12, 15 T .

The parameters studied were; field strength, pulse shape, and target size. Varies size of coils were used to provide fields of 8 to 15 Tin targets as shown in Fig. 4. A summary of all the shot days is given in Appendix A. Two pulse shapes, a 1 ns square pulse and a ramped pulse shown in Fig. 5, were used. The simulated adiabats α were 5 and 3.5, respectively. Two different target sizes, $\sim$ 860 and $\sim$ 920 μm outer diameter were used. Table I summarizes all of the experimental conditions.

V. EXPERIMENTAL RESULTS

The implosion performance was assessed through the measurement of neutron yields Y_N and neutron-averaged ion temperatures T_i, both measured using neutron time-of-flight

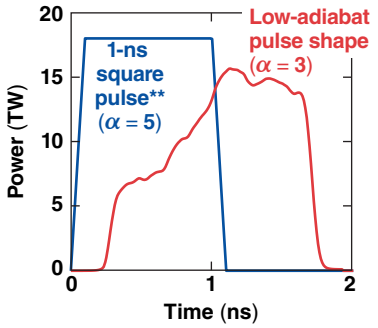

Figure 5. Two different pulse shape were used. The simulated adiabat for the 1 ns square pulse and the ramp pulse are 5 and 3.5, respectively.

#	B (T)	Coil	Pulse shape	Adiabat	E_L (kJ)
1	8	I	1ns square	5	18
2	12,15	III	1ns square	5	18
3	8	II	ramp pulse	3.5	16
4	9	II	ramp pulse	3.5	16

Table I. Summaries of the conditions for all the data. Coil types are listed in Fig. 4.

(nToF) detectors [19] situated 3 m from the target. The shell trajectories of the imploding targets were also measured using an x-ray framing camera (XRFC) [20, 21] on the 4^{th} shot day in Table I. The shell radius at different times was obtained by imaging the soft x-ray self-emission of the coronal plasma on the XRFC [22]. Shown in Fig. 6 are the radii versus time for all the shots on that day. The average velocity of the ablation front for target with outer diameters equal to ~ 860 μm were $V_{\text{imp}} = 143.0 \pm 10.2$ km/s and 131.4 ± 8.5 km/s for $B = 0$ and 9 T, respectively. The average-implosion velocity was reduced by 8.8 %, with an 80 % confidence level according to the $t-$test, by the magnetic field. The reduction of the shell velocity is not significant and is consistent with the predictions of simulations. Note that the ablation front velocity is significantly less than the shell implosion velocity.

The measured neutron yields and ion temperatures versus the initial magnetic fields B_0 are shown in Fig. 7. Large shot-to-shot variations were observed, especially in the ion temperatures. Besides magnetic field, there is no significant correlation between ion temperature and any other observable, such as shell thickness, target outer diameters, etc.

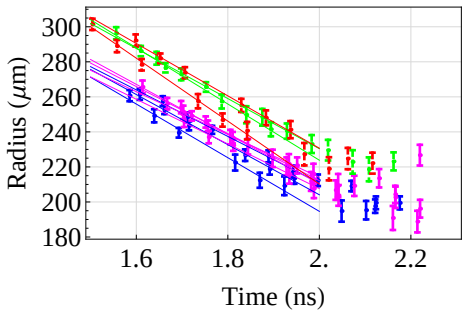

Figure 6. Radius versus time for different shots on the 4$^{\text{th}}$ shot day in Table I. The lines are curve fits to the radius and the slopes are the implosion velocities. Blue and magenta color represent the case where the outer diameter of the targets were $\sim$ 860 μm and $B = 0, 9$ T, respectively. Green and red color represent the case where the outer diameter of the targets were $\sim$ 920 μm and $B = 0, 9$ T, respectively.

The overall mean ion temperatures with and without magnetic field are 2.6 ± 0.3 keV and 2.5 ± 0.3 keV, respectively. Mean ion temperature increases by 4 %, with only 74 % confidence level using the $t-$ test, due to magnetic field. With a ± 0.5 keV uncertainty in temperature it is very hard to confirm any temperature changes within ± 20 %. Nevertheless, a trend of neutron yield increase due to the magnetic field was clearly observed.

A series of simulations using the experimental conditions, including the actual laser pulse shapes, laser energy on target, target dimensions, fill pressures, and seed magnetic fields, were conducted. The comparison between the experimental and the simulation results are shown in Fig. 8. In the simulations, the predicted neutron yields are higher using the ramped pulse than the 1 ns square pulse. However, the measured neutron yields are comparable or even lower using the ramped pulse, and they are both lower than the simulations. Neutron yield is degraded due to perturbation growth in the deceleration phase, which is not modeled in the 1.5-D simulation, nor captured in x-ray back-lighted images taken a few 100 ps before peak compression [4]. Shown in Fig. 9 is an image from the filtered, gated, monochromatic x-ray imager (GMXI) [23] (channel D with $h\nu \sim 5$ keV) for shot number 73054 on the 4$^{\text{th}}$ shot day. In this particular shot, the hot spot is strongly distorted and the neutron yield is relatively low. With lower adiabat, the Rayleigh–Taylor (RT) instability at the shell outer surface grows faster during the acceleration phase [24]. The instability eventually seeds the perturbation at the shell inner surface and degrades the target performance so that the

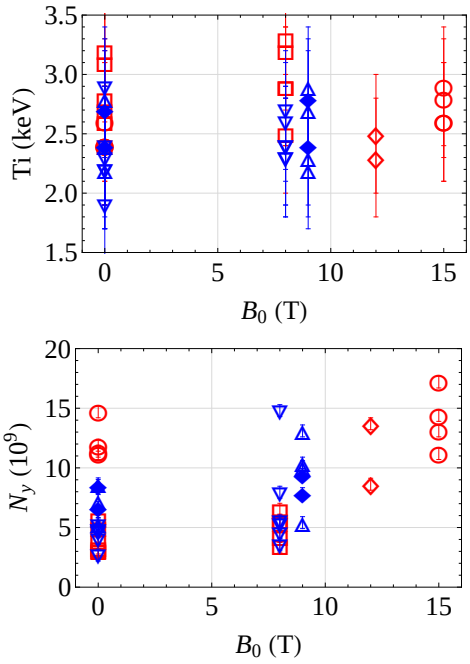

Figure 7. The target outer diameters for solid diamonds were 920 μm while they were 860 μm for all the other experiments. (1) The red squares are for B = 0/8 T and $\alpha = 5$. (2) The red diamonds are for B = 0/12 T and $\alpha = 5$. (3) The red circles are for B = 0/15 T and $\alpha = 5$. (4) The blue down-triangles are for B = 0/8 T and $\alpha = 3.5$. (5) The blue up-triangles are for B = 0/9 T and $\alpha = 3.5$. (6) The blue solid diamonds are for B = 0/9 T and $\alpha = 3.5$.

measured neutron yield using the ramped pulse is slightly lower than using 1 ns square pulse even though it is predicted to be higher. The predicted neutron averaged ion temperature increased about 0.3 keV in simulations. However, due to large shot to shot variations the trend in temperature enhancement is difficult to measure in experiments. The error bar in mean ion temperatures is 0.5 keV, which is larger than the predicted increase.

Neutron yields versus shell thickness are plotted in Fig. 10, since neutron yield decreases with thicker shells due to the lower implosion velocity [25]. To separate the effects of magnetic field, shell thickness and adiabat, multiple linear regression has been used. All of the data can be fitted using a single expression

$$Y_{\rm n}\left(\times 10^9\right) = Y_{\rm n0} + A_{\rm B}B_0 + A_\Delta \Delta + A_\alpha \alpha \tag{10}$$

where B_0 is seed magnetic field (from 0 to 15 T), Δ is shell thickness, and α is adiabat (3.5 or 5). A least-squares fit to the data gives the fitting parameters: $Y_{\rm n0}\left(\times 10^9\right) = 76.4 \pm 15.2$,

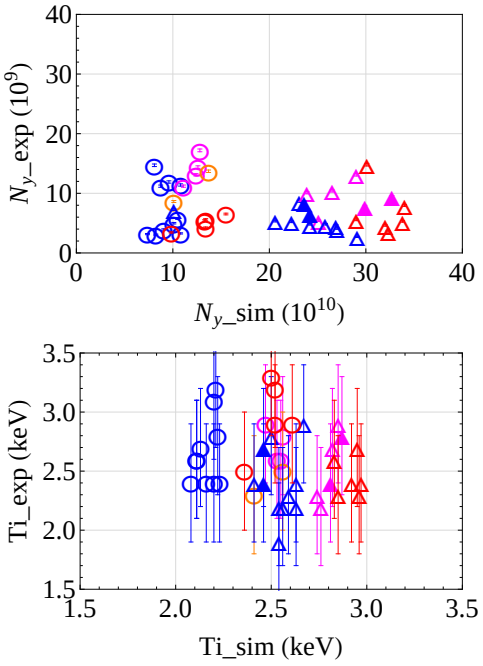

Figure 8. Comparisons of (a) the neutron yield and (b) neutron average ion temperature between the experimental and the simulation results. The target outer diameters for solid triangles were 920 μm while they were 860 μm for all the other experiments. (1) The blue, red, orange, magenta circles are for $\alpha = 5$ and B = 0/8/12/15 T, respectively. (2) The blue, red, and magenta open triangles are for $\alpha = 3.5$ and B = 0/8/9 T, respectively. (3) The blue and magenta solid triangles are for $\alpha = 3.5$ and B = 0/9 T, respectively.

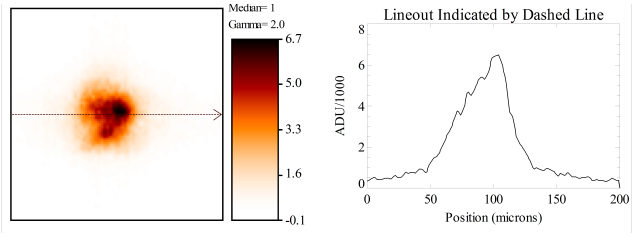

Figure 9. GMXI channel D ($h\nu \sim 5$ keV) image in a region of 200 μm $\times$ 200 μm for shot 73054.

$A_{\rm B}\,(1/{\rm T}) = 0.28\pm0.09$, $A_\Delta\,(1/\mu m) = -3.48\pm0.73$, and $A_\alpha = 2.55\pm0.70$. The $t-$test shows that the confidence level for $Y_{\rm n0}$, $A_{\rm B}$, A_Δ, and A_α are all above 99 %. The regression results are also plotted in Fig. 10. For shell thickness equal to 21.5 μm, which gives the lowest yield enhancement, the neutron yields increased by 35 % and 30 % for $\alpha = 5$, ${\rm B}_0 = 15$ T and $\alpha = 3.5$, ${\rm B}_0 = 9$ T, respectively. Adding a magnetic field leads to higher neutron yield,

but fields higher than 8 T do not give further yield enhancement.

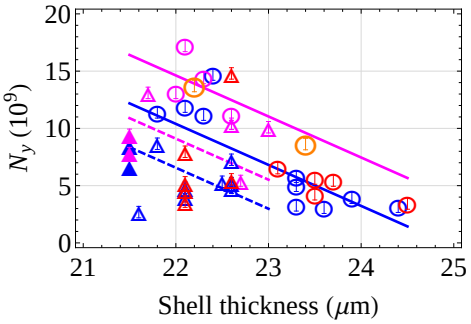

Figure 10. The target outer diameters for solid triangles were 920 μm while they were 860 μm for all the other experiments. (1) The blue, red, orange, magenta circles are for $\alpha = 5$ and $B = 0, 8, 12, 15$ T, respectively. (2) The blue, red, and magenta open triangles are for $\alpha = 3.5$ and $B = 0, 8, 9$ T, respectively. (3) The blue and magenta solid triangles are for $\alpha = 3.5$ and $B = 0, 9$ T, respectively. (4) The lines are from the regression results using Eq. 10. The solid lines are for $\alpha = 5$ while the dashed lines are for $\alpha = 3.5$. Both blue lines are for $B_0 = 0$ T while solid magenta line is for $B_0 = 15$ T and dashed magenta line is for $B_0 = 9$ T.

To check the consistency between the yield enhancement and the uncertainty in the ion temperature increase, we can use the scaling law for neutron yield

$$Y_{\rm n} \sim n^2 \langle \sigma v \rangle V \sim p^2 T^2 V \tag{11}$$

where $\langle \sigma v \rangle \sim T^4$ in the temperature range of 2 to 5 keV is used. For neutron yield increasing by $\sim$ 30 %, the corresponding temperature increase is $\sim$ 15 %, which is smaller than the measurement uncertainty. Therefore, the ion temperature increase does not conflict with the neutron yield enhancement.

VI. CONCLUSIONS

Simulations of magnetized implosions on OMEGA show that the field can be compressed to more than 200 times higher conserving 80 % of the magnetic flux. However, the plasma β is much larger than unity so the hydrodynamic compression is not influenced directly by the magnetic field. The magnetic field in the corona is convected away by the laser ablation. The field between the critical surface and ablation surface is decreased and it does not change

the thermal conductivity in the corona. Therefore no significant impact on shell trajectory is expected. Instead, the magnetic field in the hot spot is compressed to large enough values to reduce thermal conductivity, increasing neutron yield and ion temperature.

In experiments, shell trajectories, neutron-averaged ion temperatures and neutron yields were measured. The ablation front velocity calculated from shell trajectories shows a 8 % reduction with the field compared to the case without field with only 80 % confidence level. This is consistent with the prediction from simulations where no significant difference in shell trajectories with and without magnetic field is observed. Large shot-to-shot variations and significant error bars in the ion temperature measurements make it practically impossible to observe the expected increase in ion temperature with magnetization. Nevertheless, multiple linear regression shows that the neutron yield increases with magnetic field with a confidence level above 99 %. For shell thickness of 21.5 μm, which gives the lowest yield enhancement, the neutron yields increase by 35 % and 30 % for $\alpha = 5$, $B_0 = 15$ T and $\alpha = 3.5$, $B_0 = 9$ T, respectively.

From the experimental results, we can conclude that the neutron yield is definitely enhanced with a seed field in the target. However, fields higher than 8 T do not lead to greater yield enhancement. To observe the predicted ion temperature increase, the uncertainty of the ion temperature measurement and the shot-to-shot variation need to be reduced. With the open-field-line configuration, the largest reduction in thermal conductivity is by a factor of two. To fully suppress heat conduction requires a closed-field-line configuration, but this is not possible by external means with a spherical target. The simplest approach to reach this limit with the existing capabilities on OMEGA is to use cylindrical targets. The first MIFEDS experiments with cylinders gave low neutron yield [2, 3], but a new approach is now being developed based on the magnetized liner inertial fusion scheme (MagLIF) [26], where the gas fill will be preheated, which is expected to considerably enhance the yield.

APPENDIX A

Date	B (T)	P (atm)	Pulse shape	Adiabat	E_L (kJ)	Purpose
2010/11/23	8	10	1ns square	5	18	Yield enhancement
2011/11/15	3	5	1ns square	5	18	Yield enhancement
2013/ 2/13	6	20	1ns square	5	16.9	Field measurement
2013/ 4/17	8	10	ramp pulse	3	16	Yield enhancement
2014/ 2/ 6	5	20	1ns square	5	16.9	Field measurement
2014/ 4/17	9	10	ramp pulse	3	16	Yield enhancement
2014/ 7/16	12,15	10	1ns square	5	18	Yield enhancement

Table II. Summary of all the shot days.

[1] R. Betti and C. Zhou, Physics of Plasmas **12**, 110702 (2005).

[2] J. P. Knauer, O. V. Gotchev, P. Y. Chang, D. D. Meyerhofer, O. Polomarov, R. Betti, J. A. Frenje, C. K. Li, M. J.-E. Manuel, R. D. Petrasso, J. R. Rygg, and F. H. Seguin, Physics of Plasmas **17**, 056318 (2010).

[3] O. V. Gotchev, P. Y. Chang, J. P. Knauer, D. D. Meyerhofer, O. Polomarov, J. Frenje, C. K. Li, M. J. E. Manuel, R. D. Petrasso, J. R. Rygg, F. H. Seguin, and R. Betti, Phys. Rev. Lett. **103**, 215004 (2009).

[4] P. Y. Chang, G. Fiksel, M. Hohenberger, J. P. Knauer, R. Betti, F. J. Marshall, D. D. Meyerhofer, F. H. Seguin, and R. D. Petrasso, Phys. Rev. Lett. **107**, 035006 (2011).

[5] S. I. Braginskii, Review of Plasma Physics **1**, 205 (1965).

[6] J. Delettrez and E. B. Goldman, *Laboratory for Laser Energetics Report No. 36, University of Rochester; NTIS document No. DOE/SF/19460-118*, Tech. Rep. (1976).

[7] T. Boehly, D. Brown, R. Craxton, R. Keck, J. Knauer, J. Kelly, T. Kessler, S. Kumpan, S. Loucks, S. Letzring, F. Marshall, R. McCrory, S. Morse, W. Seka, J. Soures, and C. Verdon, Optics Communications **133**, 495 (1997).

[8] C. D. Zhou and R. Betti, Physics of Plasmas **15**, 102707 (2008).

[9] J. Delettrez, R. Epstein, M. C. Richardson, P. A. Jaanimagi, and B. L. Henke, Phys. Rev. A **36**, 3926 (1987).

[10] S. P. Lyon and J. D. Johnson, *EOS For Polycrystalline Quartz.*, Tech. Rep. (Los Alamos National Laboratory Report No. LA-UR-92-3407, 1985).

[11] A. Nishiguchi, T. Yabe, and M. G. Haines, Physics of Fluids **28**, 3683 (1985).

[12] J. R. Davies, R. Betti, P.-Y. Chang, and G. Fiksel, Physics of Plasmas **22**, 112703 (2015).

[13] S. Skupsky, J. A. Marozas, R. S. Craxton, R. Betti, T. J. B. Collins, J. A. Delettrez, V. N. Goncharov, P. W. McKenty, P. B. Radha, T. R. Boehly, J. P. Knauer, F. J. Marshall, D. R. Harding, J. D. Kilkenny, D. D. Meyerhofer, T. C. Sangster, and R. L. McCrory, Physics of Plasmas (1994-present) **11**, 2763 (2004).

[14] R. S. Craxton, F. J. Marshall, M. J. Bonino, R. Epstein, P. W. McKenty, S. Skupsky, J. A. Delettrez, I. V. Igumenshchev, D. W. Jacobs-Perkins, J. P. Knauer, J. A. Marozas, P. B. Radha, and W. Seka, Physics of Plasmas (1994-present) **12**, 056304 (2005).

[15] F. Marshall, R. Craxton, M. Bonino, R. Epstein, V. Glebov, D. Jacobs-Perkins, J. Knauer, J.A.Marozas, P. McKenty, S. Noyes, P. Radha, W. Seka, S. Skupsky, and V. Smalyuk, J. Phys. IV France **133**, 153 (2006).

[16] F. J. Marshall, P. W. McKenty, J. A. Delettrez, R. Epstein, J. P. Knauer, V. A. Smalyuk, J. A. Frenje, C. K. Li, R. D. Petrasso, F. H. Séguin, and R. C. Mancini, Phys. Rev. Lett. **102**, 185004 (2009).

[17] O. V. Gotchev, J. P. Knauer, P. Y. Chang, N. W. Jang, M. J. Shoup, III, D. D. Meyerhofer, and R. Betti, Review of Scientific Instruments **80**, 043504 (2009).

[18] G. Fiksel, A. Agliata, D. Barnak, G. Brent, P.-Y. Chang, L. Folnsbee, G. Gates, D. Hasset, D. Lonobile, J. Magoon, D. Mastrosimone, M. J. Shoup, and R. Betti, Review of Scientific Instruments **86**, 016105 (2015).

[19] V. Y. Glebov, D. D. Meyerhofer, T. C. Sangster, C. Stoeckl, S. Roberts, C. A. Barrera, J. R. Celeste, C. J. Cerjan, L. S. Dauffy, D. C. Eder, R. L. Griffith, S. W. Haan, B. A. Hammel, S. P. Hatchett, N. Izumi, J. R. Kimbrough, J. A. Koch, O. L. Landen, R. A. Lerche, B. J. MacGowan, M. J. Moran, E. W. Ng, T. W. Phillips, P. M. Song, R. Tommasini, B. K. Young, S. E. Caldwell, G. P. Grim, S. C. Evans, J. M. Mack, T. J. Sedillo, M. D. Wilke, D. C. Wilson, C. S. Young, D. Casey, J. A. Frenje, C. K. Li, R. D. Petrasso, F. H. SÃ©guin, J. L. Bourgade, L. Disdier, M. Houry, I. Lantuejoul, O. Landoas, G. A. Chandler, G. W. Cooper, R. J. Leeper,

R. E. Olson, C. L. Ruiz, M. A. Sweeney, S. P. Padalino, C. Horsfield, and B. A. Davis, Review of Scientific Instruments **77**, 10E715 (2006).

[20] D. K. Bradley, P. M. Bell, J. D. Kilkenny, R. Hanks, O. Landen, P. A. Jaanimagi, P. W. McKenty, and C. P. Verdon, Review of Scientific Instruments **63**, 4813 (1992).

[21] D. K. Bradley, P. M. Bell, O. L. Landen, J. D. Kilkenny, and J. Oertel, Review of Scientific Instruments **66**, 716 (1995).

[22] D. T. Michel, C. Sorce, R. Epstein, N. Whiting, I. V. Igumenshchev, R. Jungquist, and D. H. Froula, Review of Scientific Instruments **83**, 10E530 (2012).

[23] F. J. Marshall and J. A. Oertel, Review of Scientific Instruments **68**, 735 (1997).

[24] K. Anderson and R. Betti, Physics of Plasmas **10**, 4448 (2003).

[25] F. J. Marshall, J. A. Delettrez, V. Y. Glebov, R. P. J. Town, B. Yaakobi, R. L. Kremens, and M. Cable, Physics of Plasmas **7**, 1006 (2000).

[26] S. A. Slutz, M. C. Herrmann, R. A. Vesey, A. B. Sefkow, D. B. Sinars, D. C. Rovang, K. J. Peterson, and M. E. Cuneo, Physics of Plasmas **17**, 056303 (2010).